

# Lawrence Berkeley National Laboratory

## LBL Publications

### Title

Exploiting heat transfer to achieve efficient photoelectrochemical CO<sub>2</sub> reduction under light concentration

### Permalink

<https://escholarship.org/uc/item/5x73x034>

### Journal

Energy & Environmental Science, 15(5)

### ISSN

1754-5692

### Authors

Kistler, Tobias A  
Um, Min Young  
Cooper, Jason K  
[et al.](#)

### Publication Date

2022-05-18

### DOI

10.1039/d1ee03957a

Peer reviewed

1 **Exploiting Heat Transfer to Achieve Efficient Photoelectrochemical CO<sub>2</sub> Reduction**  
2 **under Light Concentration**

3

4 Tobias A. Kistler<sup>1,2,3</sup>, Min Young Um<sup>1,2</sup>, Jason K. Cooper<sup>1,2</sup>, Ian D. Sharp<sup>3</sup>, Peter Agbo<sup>1,2,\*</sup>

5

6 <sup>1</sup>Chemical Sciences Division, Lawrence Berkeley National Laboratory, Berkeley, California

7 94720, USA

8 <sup>2</sup>Joint Center for Artificial Photosynthesis, Lawrence Berkeley National Laboratory, Berkeley,

9 California 94720, USA

10 <sup>3</sup>Walter Schottky Institute and Physics Department, Technische Universität München, 85748

11 Garching, Germany

12

13 \*Corresponding Author: pagbo@lbl.gov

14 **Abstract**

15 Photoelectrochemical (PEC) conversion of carbon dioxide into valuable chemicals and fuels  
16 represents a promising path towards combating anthropogenic CO<sub>2</sub> emissions. However, the  
17 limited conversion efficiencies, operation lifetimes and CO<sub>2</sub> utilization efficiencies of PEC  
18 devices currently prohibit their application beyond the laboratory scale. Here, a wireless  
19 device converting CO<sub>2</sub> and water into carbon monoxide and hydrogen at a peak solar  
20 conversion efficiency exceeding 16% under an illumination intensity of 5 suns is  
21 demonstrated. A CO/H<sub>2</sub> product ratio between 10 - 20 is measured during a 17 h stability test.  
22 Fluctuations in device performance are rigorously analyzed via deconvolution of  
23 electrochemical and photoabsorber contributions. It is demonstrated that beneficial heat  
24 dissipation is enabled by wireless integration of the photoabsorber and electrocatalyst  
25 components, accounting for roughly 10% of the achieved conversion efficiency, an  
26 achievement unattainable with physically separated photoabsorber and electrolyzer  
27 components.

## 28 **Introduction**

29           While mean planetary temperatures continue to rise due to increasing anthropogenic  
30 carbon dioxide emissions, many countries still depend heavily on fossil fuels.<sup>1,2</sup> Converting  
31 exhaust CO<sub>2</sub> into fuels and other valuable chemicals provides a promising pathway to reduce  
32 the impacts of climate change and move away from fossil fuels. Electrochemical (EC) CO<sub>2</sub>  
33 reduction is one of several options for industrial-scale CO<sub>2</sub> conversion.<sup>3,4</sup> Ideally, such a  
34 process will be driven by renewable energy sources such as wind or sunlight.

35           Solar-driven CO<sub>2</sub> reduction may be facilitated by connecting a photovoltaic (PV)  
36 element to a dark electrolyzer. Yet, these designs generally do not exploit the potential heat  
37 exchange between the photoabsorber and electrolyte, which is expected to improve the overall  
38 efficiency in fully-integrated, photoelectrochemical (PEC) cells. Such heat exchange is  
39 especially important when concentrated sunlight is used to illuminate the photoabsorber.<sup>5</sup>  
40 Liquid electrolyte that flows through the electrolyzer cools the PV, significantly increasing its  
41 efficiency at elevated light concentrations. The heated electrolyte subsequently raises the  
42 temperature of catalytically active sites, improving the reaction kinetics. While conceptually  
43 promising, to date this beneficial heat exchange has rarely been demonstrated in PEC cells,  
44 due to system complexity and insufficient data collection and analysis.<sup>5</sup>

45           Until now, systems consisting of physically separated PV and electrolyzer components  
46 have outperformed wireless, PEC devices. Solar-to-fuel (STF) conversion efficiencies up to  
47 20% have been demonstrated with the former at 1 sun illumination intensity,<sup>6-13</sup> while the  
48 latter have reached only 10%.<sup>14-17</sup> Integration of the photoabsorber into the strongly alkaline  
49 environment usually present in CO<sub>2</sub> electrolyzers introduces durability challenges, hindering  
50 the employment of beneficial device design strategies developed for dark CO<sub>2</sub> electrolysis. So  
51 far there have been very few reports of membrane-electrode assembly (MEA)-type, PEC

52 devices for CO<sub>2</sub> reduction,<sup>14,18</sup> despite persuasive arguments that MEA devices can offer lower  
53 operating voltages than corresponding flow cells, with potentially increased lifetimes.<sup>19,20</sup>  
54 Similarly, there have been very few demonstrations of solar-driven CO<sub>2</sub> electrolysis using  
55 concentrated sunlight, even though semiconductor photoabsorbers are generally more efficient  
56 under modest light concentration if sufficient cooling is provided and the series resistance is  
57 low enough.<sup>21-26</sup>

58 Here, we describe a fully-integrated, wireless, PEC device converting CO<sub>2</sub> to carbon  
59 monoxide at a peak solar-to-CO (STCO) efficiency of 15%, while producing hydrogen at a  
60 solar-to-H<sub>2</sub> (STH) efficiency of 1%, resulting in a combined STF efficiency of 16%. This  
61 marks a 60% improvement in STF efficiency relative to previous reports of fully-integrated,  
62 wireless, PEC devices for CO<sub>2</sub> conversion.<sup>14-17</sup> During a 17 h trial, the CO/H<sub>2</sub> product ratio  
63 ranges between 20:1 and 10:1 with no permanent degradation observed in device  
64 performance. Fluctuations in the combined STF efficiency between 6% and 16% are shown to  
65 be the result of bubble accumulation in the relatively thick anode layer. Stability tests revealed  
66 that the photoabsorber temperature plays an important role for the STF efficiency, especially  
67 when the operating point lies near the maximum power point (MPP) of the PV. Consequently,  
68 by analyzing the operating current and voltage, we demonstrate how PV cooling via liquid  
69 electrolyte enabled noteworthy device performance enhancements.

70

## 71 **Results and Discussion**

### 72 **Device architecture**

73 At the center of our device lies the PV-integrated membrane (PIM), consisting of a  
74 triple-junction PV surrounded by a Selemon membrane, as detailed in previous reports<sup>14,27</sup>  
75 (Fig. 1a and Fig. 1c). Similar to a MEA, the PIM is sandwiched by two carbon paper

76 substrates coated with catalysts, leaving the PV unobstructed. On the cathode side, a gold  
77 catalyst is deposited on a micro-porous layer (MPL) containing polytetrafluoroethylene,  
78 which creates a hydrophobic micro-environment on the gas diffusion electrode.<sup>28</sup> Humidified  
79 CO<sub>2</sub> flows through the serpentine channels in the acrylic front endplate and diffuses through  
80 the carbon paper towards the catalyst. On the catalyst surface, CO<sub>2</sub> and H<sub>2</sub>O are converted to  
81 CO and H<sub>2</sub>, depending on local reaction conditions,<sup>14,28-31</sup> while generating hydroxide ions that  
82 diffuse through the anion exchange membrane and react to form O<sub>2</sub> on the anodic catalyst  
83 surface. On the anode side, the Ni catalyst is directly sputtered on the carbon fibers (no MPL),  
84 creating a more hydrophilic environment than at the cathode. This allows the potassium  
85 hydroxide anolyte to wet the surface of the catalyst as it flows through channels machined in  
86 the anodic endplate.

87         The PV sits in the middle of the catalytic structure and can be directly illuminated  
88 through the acrylic endplate (cathode side), reducing path-dependent light attenuation  
89 compared to devices that include catalysts or electrolytes in the illumination path. However,  
90 since the catalyst is placed around the PV, the effective illumination area (with respect to the  
91 overall device footprint) is reduced unless a lens is used to concentrate the light that would  
92 otherwise fall on the carbon paper onto the PV (Fig. 1b). Furthermore, employment of a lens  
93 may significantly reduce the material costs, as the area of the high-efficiency photoabsorber  
94 can be reduced compared to the total illumination area. The light concentration factor using a  
95 Fresnel lens is adjusted by changing the distance between the lens and the PEC cell (**Fig. S1**,  
96 ESI).

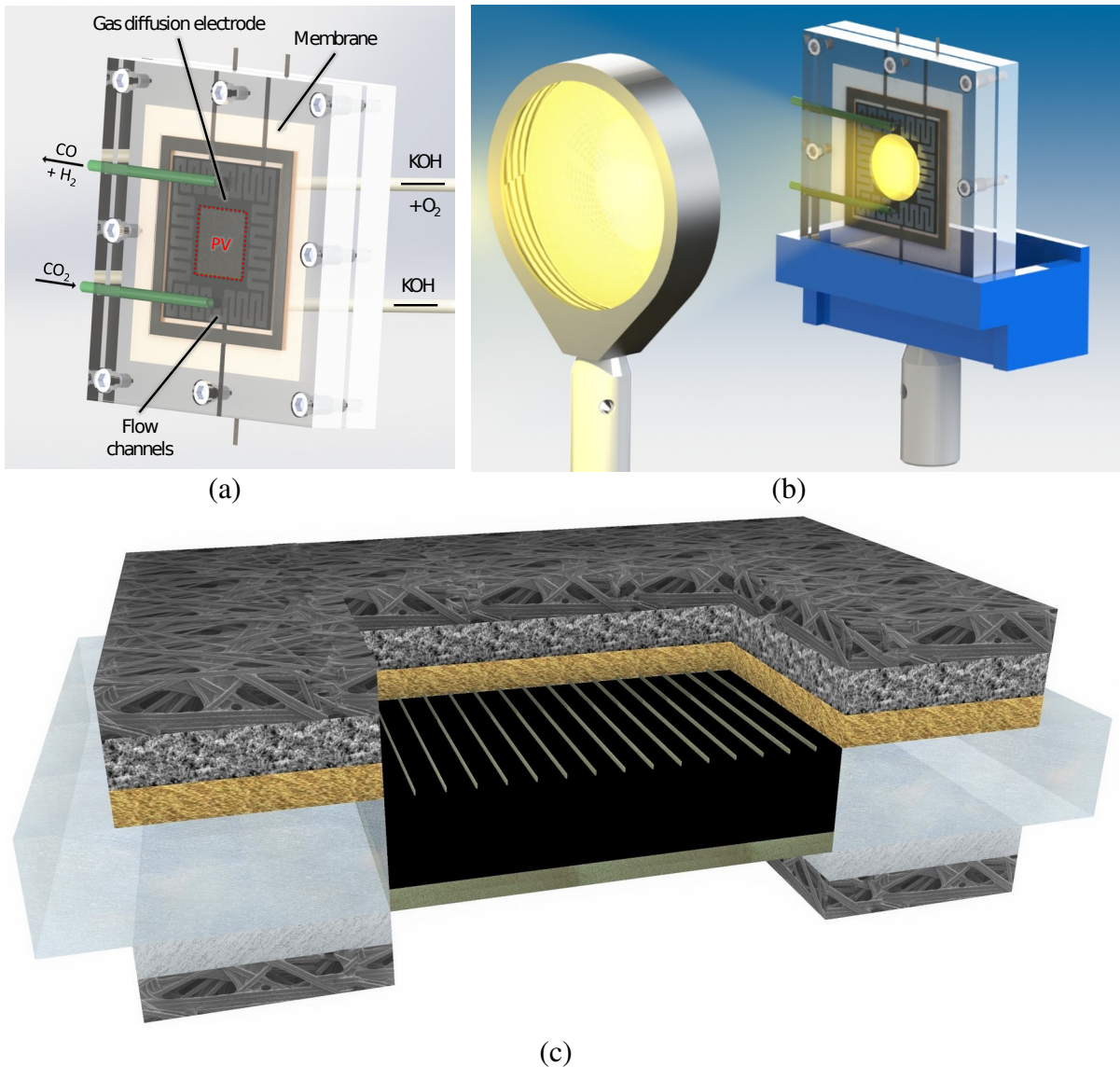


**Fig. 1.** Fully-integrated, wireless, PEC device used for light concentration testing. (a) PIM device performing PEC  $\text{CO}_2$  reduction to  $\text{CO}$  and  $\text{H}_2$ . We note that the cathode outlet stream also contains unreacted  $\text{CO}_2$  and the device design and operating conditions dictate the overall  $\text{CO}_2$  utilization. (b) Fresnel lens concentrating the incoming light onto the PV of the PIM device. Moving the (green) cathodic inlet and outlet to the side of the cell enabled closer placement of the Fresnel lens to the PEC device. (c) Cross-section image showing the operating principle of the PIM device. The chemical reactions are shown without coefficients and the thickness of the layers are not to scale.

97

98 **Electrochemical optimization for operation under light concentration**

99 During PEC operation, the catalytic, EC components are coupled directly to the PV.  
100 Electroneutrality demands that the flux of electrical currents through series-linked  
101 components must be equal. As a result, the measured device current will be determined by the  
102 current-limiting component (PV or EC). To avoid significant efficiency penalties in a PEC  
103 device due to the shape of the PV polarization curve, the achievable EC current should equal  
104 or exceed the PV short circuit current ( $I_{sc}$ ) at a voltage slightly lower than at the MPP. Here,  
105 we define a critical voltage ( $V_{crit}$ ), to prevent current drops in the PV polarization curve larger  
106 than 0.2% of  $I_{sc}$ . In other words,  $V_{crit}$  marks the point at which the PV polarization curve  
107 transitions from a flat line to an exponentially falling curve (see **Fig. S2**, ESI). In our case  $V_{crit}$   
108 is ~2.1 V.

109 As mentioned above, illumination of the non-photoactive carbon paper should be  
110 avoided to maximize fuel production per total device area. Concentrating the light onto the  
111 photoabsorber increases its total output current provided to the catalytically active sites.  
112 Therefore, increasing the light concentration while keeping the catalyst area unchanged,  
113 requires optimizing the electrochemical activity of the catalyst to enable higher catalytic  
114 current densities at the same operating voltage.

115 The minimum concentration factor ( $c$ ) to avoid losses of illumination area can be  
116 determined according to the respective areas of the catalyst ( $A_{cat}$ ) and PV ( $A_{PV}$ ):

$$117 \quad c = \frac{A_{PV} + A_{cat}}{A_{PV}}.$$

(SEQ Equation ARABIC 1)

118 This results in the expected PV current under light concentration:

$$119 \quad I_{PV} = j_{sc, 1sun} \times c \times A_{PV},$$

(SEQ Equation ARABIC 2)

120 with  $j_{sc, 1sun}$  describing the maximum achievable PV current density under short circuit  
121 conditions and 1 sun illumination intensity (no concentration).



122 Since the PV (equation 2) and EC ( $I_{EC} = j_{EC} \times A_{cat}$ ) currents need to be equal, the EC  
 123 current density ( $j_{EC}$ ) can be calculated as a function of the PV and catalyst areas:

124 
$$j_{EC} = j_{sc, 1sun} \times \left( \frac{A_{PV}}{A_{cat}} + 1 \right).$$
  
 (SEQ Equation ARABIC 3)

125 Therefore,  $j_{EC} \geq j_{sc, 1sun}$  and using the parameters of the chosen PV ( $A_{PV} = 0.94 \text{ cm}^2$ ,  $j_{sc, 1sun} =$   
 126  $12.22 \text{ mA cm}^{-2}$ ) results in the blue current density as a function of the catalyst area curve  
 127 shown in Fig. 2a.

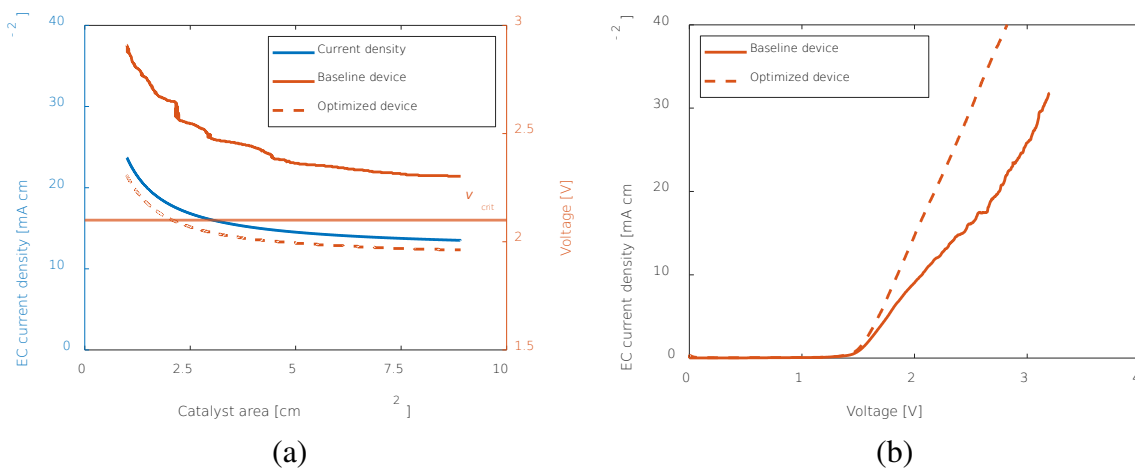


**Fig. 2.** Optimization of the EC performance. (a) Operating voltage and current density of the catalysts as a function of the geometric area. Optimization of the operating conditions for the baseline device was necessary to avoid current drops larger than 0.2% of  $I_{sc}$  by decreasing the operating voltage below  $V_{crit}$  (2.1 V). (b) EC CV curves of the baseline and optimized device, corresponding to the orange voltage curves in (a).

128 With a cyclic voltammogram (CV) measurement, the EC current density can be  
 129 determined as a function of the applied voltage (Fig. 2b). With the data from the CV and the  
 130 pre-determined current density curve from Fig. 2a, the expected operating voltage can then be  
 131 determined as a function of the catalyst area (orange curves in Fig. 2a). Even though a larger  
 132 catalyst area significantly reduces the operating voltage, using operating conditions similar to  
 133 those described previously<sup>14</sup> (baseline device) will always lead to an operating point above

134  $V_{\text{crit}}$ . Since this would result in significant efficiency penalties, the operating conditions  
135 required optimizing catalyst activity to lower the operating voltage.

136 Similar to previous studies,<sup>32–34</sup> we found that Ir and Ni perform equally well as  
137 oxygen evolution reaction catalysts under the anodic conditions used in this study (**Fig. S3**,  
138 ESI). Hence, Ni catalysts supported on carbon paper were used for all subsequent  
139 experiments. The cathode's catalytic environment was tailored through the use of an MPL on  
140 the gas diffusion electrode, which resulted in favorable performance and shifted the product  
141 distribution towards CO (**Fig. S4**, ESI). Moreover, the cathodic product ratio became  
142 independent of the cathodic inlet humidity when using the MPL (not shown here), in contrast  
143 to our previous findings without the MPL, which showed that higher humidity skewed the  
144 product distribution towards H<sub>2</sub>.<sup>14</sup> The hydrophobic nature of the MPL prevents water  
145 molecules entering the cathode chamber from reaching the catalyst sites, resulting in high CO/  
146 H<sub>2</sub> product ratios throughout a broad range of cathodic humidities.

147 In addition, raising the concentration and flow rate of the KOH anolyte increased the  
148 current at an applied potential of 2 V (**Fig. S5 and S6**, ESI). Even though 5M KOH showed  
149 the highest currents, 2M KOH provided sufficient electrochemical performance at higher flow  
150 rates, while keeping the concentration of KOH at a minimum. However, it is important to note  
151 that higher KOH flow rates lead to increased CO<sub>2</sub> crossover through the membrane,  
152 accelerating acidification of the anolyte. Such acidification may result in a rapid current  
153 degradation, when a small anolyte reservoir is used (**Fig. S7**, ESI).

154 In summary, the addition of the MPL to the cathodic gas diffusion electrode, combined  
155 with a higher KOH anolyte concentration and flow rate, increased the current by a factor of  
156 1.6-1.7 in the region of 2-2.1 V (optimized device in Fig. 2b). For a fixed PV area of 0.94 cm<sup>2</sup>,  
157 this optimized performance now allows an expected operating voltage below  $V_{\text{crit}}$  for any  
158 catalyst area larger than 2.1 cm<sup>2</sup>, with no significant voltage reductions occurring for areas

159 beyond 5 cm<sup>2</sup>. Given these considerations, we chose a catalyst area of 4 cm<sup>2</sup> to allow for small  
160 voltage fluctuations. The relative PV and EC areas thus require a light concentration factor of  
161 ~5 to minimize illumination of the non-photoactive EC element, while ensuring homogeneous  
162 illumination of the PV component in the integrated assembly.

163

#### 164 **Photoelectrochemical operation**

165 Prior to PEC operation, the PV polarization response of a fully-assembled PIM device  
166 was evaluated using an external circuit at 1, 3 and 5 suns. The short circuit current density  
167 scaled linearly with the light intensity (12.34, 36.23, and 62.07 mA cm<sup>-2</sup>, respectively), the  
168 open circuit voltage increased from 2.65 V to 2.74 V, and only a minor reduction in fill factor  
169 (< 2% sun<sup>-1</sup>) was observed (**Fig. S8**, ESI). The PV efficiency was between 27-28% for all  
170 three illumination intensities. We then added electrolyte (2M KOH, 5.9 mL min<sup>-1</sup>) and  
171 humidified CO<sub>2</sub> (60 sccm) and conditioned the catalysts by biasing the system in the dark at 2  
172 V for 50 min to achieve EC performance equilibration. This step allowed for the membrane to  
173 become equilibrated with anolyte and fully wet the cathode catalyst, which increased its  
174 electrochemically active surface area (**Fig. S9**, ESI).<sup>14,35-37</sup>

175 After equilibration, we established a direct connection between the PV and EC  
176 components to operate the PIM device in PEC mode, without external bias, at the three  
177 illumination intensities. At 1 sun, the current was stable at 12 mA during a 1 h trial, with a  
178 low operating voltage near 1.7 V due to the low EC current density needed at this light  
179 intensity (**Fig. S10**, ESI). As expected from the low operating voltage,<sup>14</sup> the product  
180 distribution heavily favored CO production, with a CO/H<sub>2</sub> product ratio near 30:1. By  
181 increasing the light intensity to 3.02 suns, the PEC current increased to 36 mA at 1.9 V (**Fig.**  
182 **S11**, ESI) and was again stable for a period of 1 h. The CO/H<sub>2</sub> product ratio was  
183 approximately the same at 30:1 as with 1-sun illumination.

184 At 5.05 suns, the optimized illumination intensity, the PIM device yielded a peak  
185 current near the short circuit current of the PV (Fig. 3a and **Fig. S12a**, ESI). The peak current  
186 was maintained for about 3 h before the current and voltage began to fluctuate. As the  
187 operating voltage rose above the voltage at the MPP ( $V_{MPP}$ ), the current dropped significantly  
188 to about 50% of its peak value due to the large gradient of the PV polarization curve in this  
189 voltage region (**Fig. S12a**, ESI). Subsequent characterization strongly suggested that these  
190 increases in operating voltage are caused by  $O_2$  bubble accumulation in the relatively thick  
191 carbon paper layer at the anode (see **Fig. S13**, ESI, Supporting Video and Experimental  
192 Section). Specifically, as the amount of trapped  $O_2$  bubbles at the anode rises, more active  
193 sites for  $O_2$  evolution are blocked, effectively reducing the catalyst surface area and increasing  
194 the operating voltage (see Fig. 2a). When these trapped bubbles are suddenly released and  
195 swept away by the flowing electrolyte, the operating voltage quickly decreases and the current  
196 recovers to its peak value (Fig. 3a). Overall, there is no irreversible current degradation  
197 observed during the 17 h trial at 5.05 suns, with a peak current density normalized by the  
198 illumination intensity of  $12.2 \text{ mA cm}^{-2} \text{ sun}^{-1}$  at an operating voltage of 2.05 V to 2.10 V. The  
199 excellent stability is further evidenced by the CVs of the PEC device before and after  
200 operation (**Fig. S12b**, ESI).

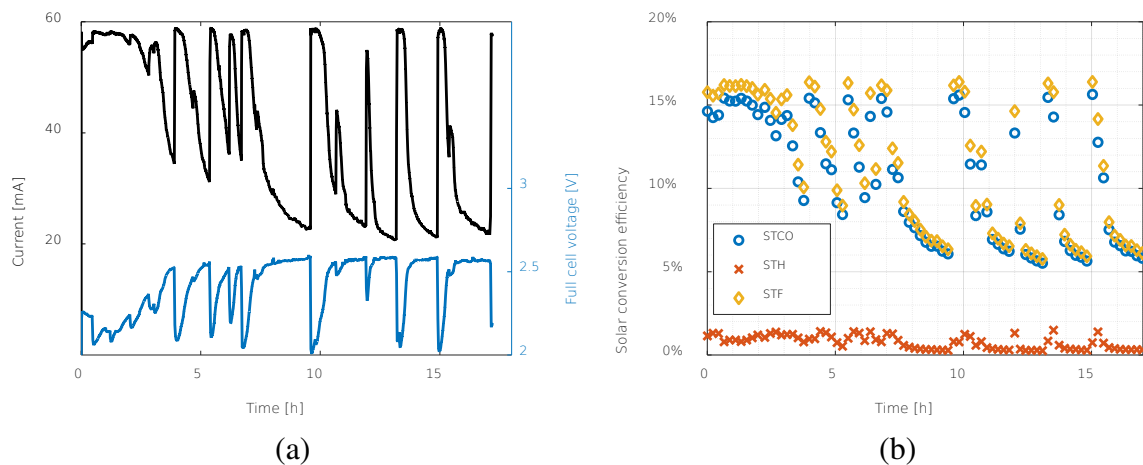


**Fig. 3.** PEC device operation for 17 h at 5.05 suns illumination intensity without external

bias. (a) Operating current and voltage. (b) STF energy conversion efficiencies.

201 The combined faradaic efficiency for CO and H<sub>2</sub> remained near 1 throughout the 17 h  
202 test, with a CO/H<sub>2</sub> product ratio ranging between 10:1 and 20:1 and an energy efficiency  
203 between 51-65% (**Fig. S12c-e**, ESI and Experimental Section). The slightly increased fraction  
204 of produced H<sub>2</sub> can be explained by the higher operating voltage compared to the 1- and 3-sun  
205 trials.<sup>14</sup> In particular, **Fig. S14** (ESI) shows the voltage dependence of the product ratio during  
206 this 17 h test. As the voltage increases, the product ratio moves towards increased H<sub>2</sub>  
207 generation until a turning point is reached near the  $V_{MPP}$  when the current starts to drop  
208 quickly. Therefore, for achieving both high currents and high CO/H<sub>2</sub> product ratios, it is  
209 important to maintain a low operating voltage.

210 With the amount of produced H<sub>2</sub> and CO, the respective solar conversion efficiencies  
211 can be calculated. The resulting STH efficiency is stable around 1% and the STCO efficiency  
212 ranges between 5.5-15.5% with a combined STF efficiency peak at 16.4% (Fig. 3b). The  
213 measured STF peak value marks a 60% relative increase compared to previous reports of  
214 fully-integrated, wireless, PEC devices.<sup>14-17</sup> In addition, it lies just below the theoretical  
215 maximum of 16.6%, as given by the PV short circuit current density measured directly after  
216 the 17 h trial and assuming a faradaic efficiency for CO of 100% (see Experimental Section  
217 and **Fig. S12a**, ESI).

218 Due to the high CO<sub>2</sub> flow rate used for this experiment, CO<sub>2</sub> utilization efficiencies  
219 were below 1%. However, CO<sub>2</sub> utilization efficiencies above 20% were achieved by reducing  
220 the CO<sub>2</sub> flow rate, with minimal reductions to the device current (~5%) (**Fig. S15**, ESI).  
221 Dilution of the CO<sub>2</sub> stream with N<sub>2</sub> at 10 sccm total flow rate also increased the CO<sub>2</sub>  
222 utilization by a factor of 5, with a 5% CO<sub>2</sub> feed showing the highest CO<sub>2</sub> utilization of 11%  
223 (**Fig. S16**, ESI).

224

## 225 **Performance gains revealed through current-voltage analysis**

226 As shown above in Fig. 3a, the operating current and voltage fluctuate considerably  
227 during the 17 h of PEC operation. Simultaneous collection of current and voltage data during  
228 steady-state operation (rather than merely logging device current over time) provides extra  
229 insight into device behavior and loss contributors.<sup>38</sup> In particular, the intersection of PV and  
230 EC performance curves indicates the expected operating point of the full PEC device at the  
231 beginning and end of operation (Fig. 4a and **Fig. S17a**, ESI). Similarly, concurrent  
232 measurement of voltage and current enables live tracking of the PEC operating point during  
233 unbiased operation. In this work, current logging is enabled by rerouting the electrons  
234 collected at the PV front surface through a potentiostat (shunt path)<sup>27</sup> before they hit the  
235 cathodic catalyst layer. The operating voltage can be measured between the PV front and back  
236 surface.

237 Any current deviation from the  $I_{sc}$  results in a performance decrease of the system.  
238 Similar to a previously disclosed method,<sup>38</sup> the encountered current losses may be  
239 deconvoluted into EC- and PV-related sources, provided that current and voltage are logged  
240 simultaneously, as described below. We note that, in contrast to our previously reported  
241 method, here the operating point is matched with a fitted EC curve instead of fitting a PV  
242 curve, which would require an assumption of unchanging, characteristic PV parameters such  
243 as shunt and series resistance during PEC device operation. PV fitting works well if it can be  
244 assumed that the PV temperature is constant and if its performance is mostly affected by  
245 partial shading, but EC fitting is preferred when the PV temperature over time is unknown.

246 As described above, bubble accumulation in the anode is likely the primary driving  
247 force for the elevated operating voltages. An increased amount of trapped bubbles will  
248 therefore reduce the usable area for catalysis, resulting in EC-related losses. Consequently, as  
249 a first deconvolution step, an EC curve is fitted through every measured operating point. For

250 this fitting process, the EC curve shown in Fig. 4a is taken as a reference and then scaled by a  
251 factor that represents the percentage of usable EC surface area compared to the reference case,  
252 yielding EC curves intersecting with the extracted operating points. The resulting percentage  
253 of usable EC area was found to range from 25-125% (**Fig. S17b**, ESI). It should be noted that  
254 the reference case for the EC curve does not represent the highest possible polarization  
255 response for the electrocatalyst layer, allowing for the determination of relative, active areas  
256 over 100%.

257 After fitting the operating point to an appropriate EC curve, PV current losses may be  
258 determined by the difference of the measured current during operation and the corresponding  
259 current on the same EC curve but at the intersection with the initial PV curve ( $I_{\text{init}}$ , **Fig. 4b**).  
260 EC losses are then calculated by subtracting  $I_{\text{init}}$  from the current on the initial PV curve at  
261 1.33 V, which is the minimum (thermodynamic) potential required for reducing CO<sub>2</sub> to  
262 CO.<sup>39,40</sup> While an increase in operating voltage naturally results in higher EC losses, it also  
263 makes the PEC device performance more susceptible to changes in the PV fill factor due to  
264 temperature fluctuations.

265 During the 17 h of operation, the operating point fluctuates in the range bounded by  
266 the PV curves measured before and after operation (Fig. 4a). While it is difficult to determine  
267 the temperature of the PV in the PEC cell assembly, measurements of the PV temperature in  
268 the reference cell indicate a logarithmic increase over time as soon as the PV is illuminated,  
269 concurrent with a drop in PV fill factor (**Fig. S18**, ESI). Since both EC and PV losses are  
270 found to be essentially reversible, PV losses are most likely caused by PV heating, while EC  
271 losses are the result of catalyst overpotential increases due to bubble accumulation, as  
272 described above. As shown in **Fig. 4c**, the major loss process comes from the EC component,  
273 while the PV loss contribution makes up only roughly 5% of the total during most of the  
274 duration of the experiment (**Fig. S17c**, ESI).

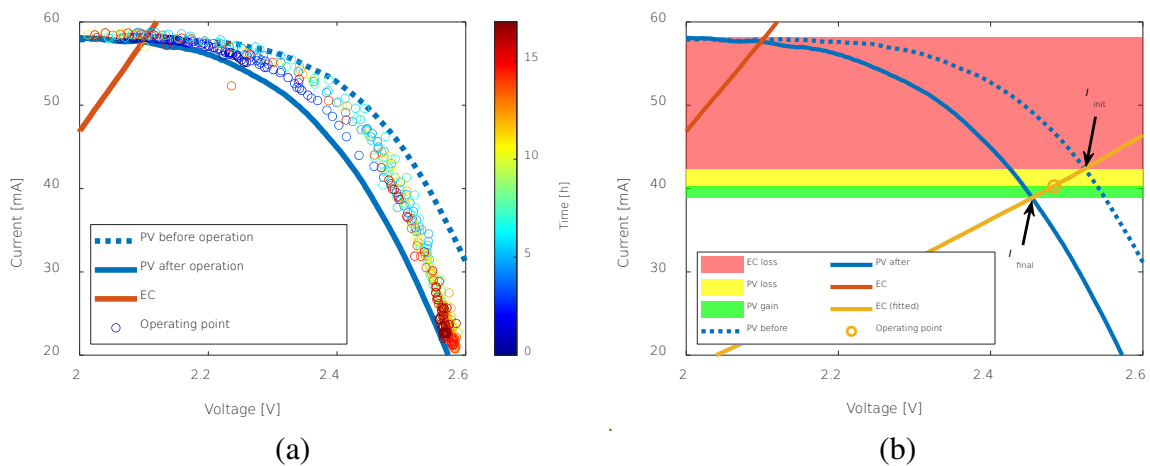
275 Interestingly, when the operating points of the PEC device during the 17 h trial are  
276 compared to the PV curve measured after the trial, the majority lie above the final PV curve.  
277 The origin of this behavior is the reduction of the PV operating temperature by convective  
278 heat transfer to the liquid electrolyte flowing through the anolyte chamber. This increases the  
279 PV efficiency in accordance with the detailed balance model developed by Shockley and  
280 Queisser<sup>41</sup> (**Fig. S19**, ESI). The resulting current gains due to lower PV temperatures may be  
281 calculated by the difference of the operating current and the corresponding current on the  
282 same EC curve but at the intersection with the final PV curve ( $I_{\text{final}}$ , **Fig. 4b**). According to the  
283 current increases, up to 5% of the achieved STF efficiency was enabled by the lower PV  
284 temperatures during operation compared to the final PV temperature after the experiment  
285 (**Fig. S20**, ESI). However, to capture the full effect of electrolyte cooling, the operating point  
286 of the PIM device should be compared to a PV curve measured without active cooling under 5  
287 suns illumination intensity (**Fig. S21**, ESI). This comparison highlights that more than 10% of  
288 the STF efficiency was enabled by cooling effects only available in a fully-integrated PEC  
289 device (**Fig. 4d**).

290 In summary, EC losses were the dominating factor for the observed current losses.  
291 Therefore, avoiding bubble accumulation in the anode chamber is the most effective way to  
292 stabilize device efficiencies. For instance, the flow channels and thickness of anodic carbon  
293 paper layer could be optimized to aid O<sub>2</sub> bubble transport. Furthermore, comparing the PEC  
294 operating point to a PV curve without active cooling highlights that more than 10% of the  
295 achieved solar conversion efficiency was enabled by cooling of the illuminated photoabsorber  
296 via electrolyte. While not described in detail here, the EC performance is also expected to  
297 benefit, in some measure, from the convective heat transfer between photoabsorber and  
298 catalyst surface facilitated by the electrolyte. Higher temperatures generally reduce the  
299 catalyst overpotential at a constant current due to the Arrhenius-type dependencies of reaction



300 kinetics.<sup>5</sup> However, it is worth noting that the electrolyte temperature increase due to  
 301 illumination is rather small for the moderate concentration levels explored by this study (**Fig.**  
 302 **S19**, ESI). Such temperature effects on reaction kinetics may become more relevant at higher  
 303 levels of illumination.

304 Finally, it should be noted that efficiency gains from PV cooling are most significant at  
 305 voltages near the MPP of the PV due to the shape of the PV polarization curve. Therefore, PV  
 306 cooling will be most effective when the catalyst overpotentials are relatively high. However,  
 307 industrially-relevant devices can be expected to be highly optimized and will likely operate  
 308 close to the MPP of the PV to reduce costs and maximize efficiency (otherwise the  
 309 photovoltage would be underutilized). Consequently, small fluctuations in catalyst  
 310 overpotential will have a larger effect on overall efficiency without PV cooling due to reduced  
 311 PV fill factors. As demonstrated in this report, beneficial heat transfer between electrolyzer  
 312 and photoabsorber components can stabilize device performance while operating near the  
 313 MPP, by keeping the PV fill factor high and reducing the catalyst overpotential.



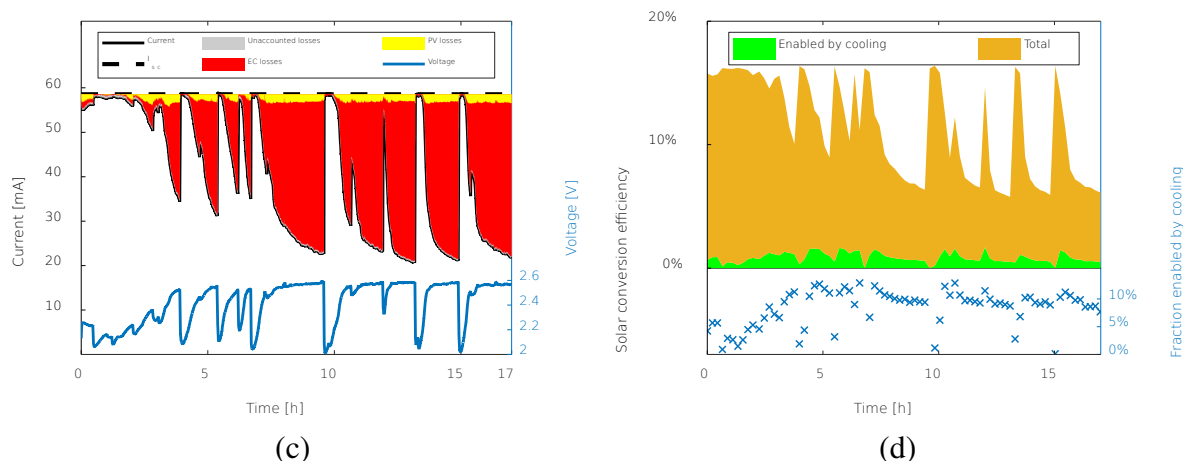


**Fig. 4.** Analysis of current fluctuations. (a) Comparison of the operating point during PEC operation to the PV and EC CV curves (see **Fig. S17a**, ESI for full-scale CVs). (b) Fitting of the EC curve to intersect with an operating point which subsequently allows specific determination of losses originating in the fully-integrated PV and EC elements. (c) Deconvoluted PV and EC losses during the 17 h trial. (d) Solar conversion efficiency of the PIM device enabled by cooling via electrolyte flow when compared to a PV without active cooling.

314

### 315 **Surface analysis after operation**

316 After the 17 h stability testing, we analyzed the surfaces of the catalyst-coated carbon  
 317 papers using scanning electron microscopy (SEM) and energy dispersive X-ray spectroscopy  
 318 (EDS). The Ni-coated carbon paper did not show any signs of degradation but the Au-coated  
 319 MPL delaminated from most of the carbon paper substrate upon device disassembly and  
 320 adhered to the membrane (**Fig. S22**, ESI). However, as long as electrical contact between the  
 321 catalyst and carbon paper substrate is maintained via mechanical compression, catalyst  
 322 adhesion to the membrane is not expected to result in performance degradation. Indeed, the  
 323 enhanced, interfacial contact between membrane and carbon paper substrate likely improves  
 324 device performance. This accords with previous findings that anion-exchange membrane  
 325 electrolyzers benefit from a catalyst coating directly on the membrane due to improved ionic

326 transport.<sup>42</sup> Finally, the range of measured CO/H<sub>2</sub> product ratios did not change much during  
327 the 17 h trial (**Fig. S12**, ESI), further indicating a stable, catalytic environment.

328

## 329 **Conclusion**

330 We demonstrated 16% STF energy conversion efficiency in a fully-integrated,  
331 wireless, PEC device at an elevated illumination intensity of 5 suns. No permanent  
332 performance degradation could be detected during a 17 h stability test. Notably, analysis of  
333 the device polarization behavior over time revealed that, on average, 10% of the measured  
334 STF efficiency was enabled by convective PV cooling in this fully-integrated structure. Such  
335 benefits would have been inaccessible when using the same materials but physically  
336 separating the photoabsorber and electrochemically active components (PV-electrolyzer  
337 configuration). Finally, with this compact device structure, CO<sub>2</sub> utilization efficiencies can be  
338 increased from 1% to 20% by simply adjusting the CO<sub>2</sub> flow rate, an important step towards  
339 commercial viability.

340

## 341 **Experimental Section**

### 342 **Deposition of catalysts**

343 Untreated Toray TGP-H-60 carbon paper (Alfa Aesar) with a thickness of 200 μm served as  
344 substrate for the anodic Ni catalyst, while a 275 μm thick carbon paper coated with a MPL  
345 (AvCarb GDS2230) was used as substrate for the cathodic Au catalyst. The MPL contains  
346 polytetrafluoroethylene particles, introducing a strongly hydrophobic characteristic to the  
347 cathodic catalyst environment. The area of the carbon paper substrates was 4 cm<sup>2</sup> shaped  
348 similarly to a window frame, leaving a gap in the center to allow for illumination of the

349 photoabsorber. All catalysts were deposited by radio frequency sputtering until a thickness of  
350 100 nm was reached with catalyst loadings of  $0.09 \text{ mg cm}^{-2}$  for Ni and  $0.19 \text{ mg cm}^{-2}$  for Au.

351

### 352 **Fabrication of the PIM and cell assembly**

353 The fabrication of the PIM has been detailed previously.<sup>14,27</sup> Briefly, a square hole is cut into  
354 the membrane to make room for the PV. Then, a combination of epoxies is used to secure the  
355 PV in the membrane and to attach Ta metal strips which enable current-voltage analysis  
356 during operation. It should be noted that the PEC cell can operate without the Ta strips, which  
357 only serve analytical purposes. Since caustic KOH was used in the anode compartment, the  
358 PV back was covered with chemically-resistant epoxy. For this study, we used Selemion  
359 AMV membranes in the chloride form ( $\sim 0.1 \text{ mm}$  thick, AGC Engineering) and III-V triple-  
360 junction PVs from Spectrolab (XTE family). The PVs show a short circuit current density of  
361  $\sim 14.07 \text{ mA cm}^{-2}$ , open circuit voltage of  $\sim 2.69 \text{ V}$ , fill factor of  $\sim 0.86$  and efficiency of  
362  $\sim 32.38\%$  at 1 sun illumination intensity and before encapsulation. The PV front and back  
363 contacts consisted of  $200 \text{ }\mu\text{m}$  thick Au layers and the PV front was covered by an anti-  
364 reflective coating. Non-transparent epoxy covered the edges of the PV, likely reducing the  
365 illuminated area of the PV to slightly less than  $0.94 \text{ cm}^2$ . In fact, the short circuit current  
366 density dropped from  $\sim 14 \text{ mA cm}^{-2}$  to  $12.62 \text{ mA cm}^{-2}$  after epoxy encapsulation. This drop in  
367 current density may be lowered by optimizing the amount of used epoxy or by deploying  
368 larger PVs where the area near the edges represents a smaller fraction of the total area.  
369 Despite some expected area losses, an illuminated area of  $0.94 \text{ cm}^2$  was considered for all  
370 efficiency calculations.

371 All cells were assembled by stacking the following layers from bottom to top: acrylic  
372 endplate with straight flow channels for the anolyte, carbon paper coated with the anodic  
373 catalyst and surrounded by a silicone gasket, PIM, Au-coated carbon paper surrounded by a

374 silicone gasket, acrylic endplate with serpentine gas flow channels. For the PEC cell, three  
375 extra layers of uncoated carbon paper were placed in between the acrylic endplate and the Ni-  
376 coated carbon paper to make enough space for the epoxy-coated PV. Alternatively, a slot can  
377 be machined into the endplates. However, if the PV does not sit perfectly in that slot,  
378 nonuniform compression can easily damage the protective coating at the edges of the PV and  
379 promote pinhole formation. Therefore, we chose to create this slot with compressible carbon  
380 paper which allows for more flexibility during cell assembly. This also required a slightly  
381 higher torque (0.18 N m) when tightening the screws of the PEC cell compared to the EC cell  
382 (0.11 N m) to prevent leaks. However, the thick layer combined with the higher torque can  
383 hinder O<sub>2</sub> bubbles from leaving the anode catalyst surface and cause bubble accumulation.

384

#### 385 **Calibration of concentrated light intensity**

386 A Newport Oriel Sol3A solar simulator equipped with a Xe lamp and AM1.5G filter was used  
387 for all illuminated experiments. To calibrate the light intensity under concentrated sunlight a  
388 Fresnel lens (2" diameter, Thorlabs FRP251) was first positioned at 1 sun illumination  
389 intensity using a monocrystalline silicon reference solar cell (Newport 91150V). The  
390 increased light intensity behind the Fresnel lens was then measured with a home-made  
391 reference cell, which mimics the composition, size and position of the photoabsorber in the  
392 PEC cell. The calibration of the home-made reference cell yielded a short circuit current  
393 density ( $j_{sc}$ ) of 12.62 mA cm<sup>-2</sup> at 1 sun and 25 °C with a temperature dependence of 0.009  
394 mA cm<sup>-2</sup> °C<sup>-1</sup>. The measured  $j_{sc}$  as a function of the distance between the reference cell and  
395 Fresnel lens can then be correlated to the light concentration factor, assuming direct  
396 proportion and correcting for the temperature ( $T$ ) as the reference cell heats up:

397 
$$c = \frac{j_{sc} - 0.009 \text{ mA cm}^{-2} \text{ } ^\circ\text{C}^{-1} \times (T - 25 \text{ } ^\circ\text{C})}{12.62 \text{ mA cm}^{-2}}$$
  
(SEQ Equation i ARABIC 4)

398

### 399 **Measurement conditions**

400 If not otherwise mentioned, the following experimental conditions were used. A peristaltic  
401 pump pushed 2M KOH at a flow rate of ~6 mL min<sup>-1</sup> through the anode chamber of the PEC  
402 cell. KOH electrolytes were prepared using ACS reagent grade pellets from Sigma-Aldrich.  
403 For all light-driven experiments, a KOH reservoir volume of ~200 mL was chosen to prevent  
404 acidification of the anolyte via CO<sub>2</sub> crossover during long-term experiments. CO<sub>2</sub> was first  
405 flowed at 60 sccm through a bubble humidifier filled with Milli-Q water (resistivity > 18.2  
406 MΩ cm) kept at room temperature (~25 °C) and then into the cathode chamber. CVs were  
407 measured in a two-electrode configuration at scan rates of 10 mV s<sup>-1</sup> for EC and PEC tests and  
408 200 mV s<sup>-1</sup> for PV tests. Dark EC stability measurements were carried out at a constant full  
409 cell potential of 2 V, while illuminated PEC tests were not biased by a potentiostat (0 V).

410

### 411 **Product analysis**

412 The cathode outlet was fed directly into a gas chromatograph from SRI Instruments (Multiple  
413 Gas Analyzer #5, 8610C) equipped with a thermal conductivity detector and flame ionization  
414 detector (FID). Prior to the FID, all products went through a methanizer to increase the  
415 minimum detection limit of the carbon-based products. The highest CO concentration  
416 available for calibration of the FID was 7980 ppm. If CO<sub>2</sub> utilization efficiencies surpass 1%,  
417 the CO concentration in the product stream will likely exceed the calibration limits.  
418 Therefore, the cathode outlet needs to be diluted with an inert gas such as argon to stay within

419 the limits and the linear range of the detector. To determine CO<sub>2</sub> utilization efficiencies, the  
420 CO molar flow in the cathode outlet stream was divided by the inlet CO<sub>2</sub> molar flow.

421

### 422 **Microscopic characterization**

423 The surface morphology and elemental composition was analyzed by SEM and EDS in an  
424 FEI Quanta 250 FEG system. An optical microscope (Olympus BX51) was used to analyze  
425 the non-conductive surface of the PIM.

426

### 427 **Conversion efficiencies**

428 With the minimum water splitting potential of 1.23 V at 25 °C, the STH efficiency can be  
429 calculated by dividing the produced H<sub>2</sub> through the illumination power density at 1 sun  
430 (0.1 W cm<sup>-2</sup>), the size of the PV (0.94 cm<sup>2</sup>) and the concentration factor:<sup>6</sup>

431

$$432 \quad STH = \frac{1.23 \text{ V} \times I_{PV} \times \text{faradaic efficiency}(H_2)}{0.1 \text{ W cm}^{-2} \times A_{PV} \times c}.$$

(SEQ Equation & ARABIC 5)

433

434 Similarly, the STCO efficiency is determined using the minimum cell potential of 1.33 V  
435 required for the cathodic evolution of CO:

436

$$437 \quad STCO = \frac{1.33 \text{ V} \times I_{PV} \times \text{faradaic efficiency}(CO)}{0.1 \text{ W cm}^{-2} \times A_{PV} \times c}.$$

(SEQ Equation & ARABIC 6)

438

439 Since no other products were observed (cumulative faradaic efficiency of measured products  
440 is near 1), the combined STF efficiency is the sum of the STH and STCO efficiencies.

441 Further, the energy/energetic efficiency (EE) towards H<sub>2</sub> and CO products is calculated via  
442 dividing the amount of energy used to form the aforementioned products by the net electrical  
443 energy supplied to the system:<sup>2</sup>

$$444 \quad EE_{H_2} = \frac{1.23 \text{ V} \times \text{faradaic efficiency}(H_2)}{\text{full cell voltage}},$$

(SEQ Equation & ARABIC 7)

$$445 \quad EE_{CO} = \frac{1.33 \text{ V} \times \text{faradaic efficiency}(CO)}{\text{full cell voltage}}.$$

(SEQ Equation & ARABIC 8)

446

## 447 **Acknowledgements**

448 The authors thank David Larson for his helpful insights and Yalili Kistler for her help with  
449 the cross-section image. This study was conducted at the Joint Center for Artificial  
450 Photosynthesis (JCAP), a DOE Energy Innovation Hub, supported through the Office of  
451 Science of the U.S. Department of Energy under Award Number DE-SC0004993. TAK  
452 acknowledges support by the German Academic Exchange Service (DAAD, No. 57504612).  
453 IDS acknowledges support by the Federal Ministry of Education and Research (BMBF,  
454 Germany) project number 033RC021B within the CO<sub>2</sub>-WIN initiative.

455

## 456 **Conflict of Interest**

457 The authors declare no competing interests.

458

## 459 **References**

- 460 1 R. U. Ayres and E. H. Ayres, *Crossing the Energy Divide. Moving from Fossil Fuel*  
461 *Dependence to a Clean-Energy Future*, Prentice Hall, Upper Saddle River, NJ, 2010.  
462 2 R. Küngas, *J. Electrochem. Soc.*, 2020, **167**, 44508.  
463 3 J. Zhang, W. Cai, F. X. Hu, H. Yang and B. Liu, *Chem. Sci.*, 2021, **12**, 6800–6819.  
464 4 S. Garg, M. Li, A. Z. Weber, L. Ge, L. Li, V. Rudolph, G. Wang and T. E. Rufford, *J.*  
465 *Mater. Chem. A*, 2020, **8**, 1511–1544.



- 466 5 S. Tembhurne, F. Nandjou and S. Haussener, *Nat. Energy*, 2019, **4**, 399–407.
- 467 6 W.-H. Cheng, M. H. Richter, I. Sullivan, D. M. Larson, C. Xiang, B. S. Brunschwig and  
468 H. A. Atwater, *ACS Energy Lett.*, 2020, **5**, 470–476.
- 469 7 M. Asadi, M. H. Motevaselian, A. Moradzadeh, L. Majidi, M. Esmaeilirad, T. V. Sun, C.  
470 Liu, R. Bose, P. Abbasi, P. Zapol, A. P. Khodadoust, L. A. Curtiss, N. R. Aluru and A.  
471 Salehi-Khojin, *Adv. Energy Mater.*, 2019, **9**, 1803536.
- 472 8 M. Schreier, F. Héroguel, L. Steier, S. Ahmad, J. S. Luterbacher, M. T. Mayer, J. Luo and  
473 M. Grätzel, *Nat. Energy*, 2017, **2**, 17087.
- 474 9 M. Schreier, L. Curvat, F. Giordano, L. Steier, A. Abate, S. M. Zakeeruddin, J. Luo, M. T.  
475 Mayer and M. Grätzel, *Nat. Commun.*, 2015, **6**, 7326.
- 476 10 G. Gurudayal, J. Bullock, D. F. Srankó, C. M. Towle, Y. Lum, M. Hettick, M. C. Scott, A.  
477 Javey and J. Ager, *Energy Environ. Sci.*, 2017, **10**, 2222–2230.
- 478 11 F. Urbain, P. Tang, N. M. Carretero, T. Andreu, L. G. Gerling, C. Voz, J. Arbiol and J. R.  
479 Morante, *Energy Environ. Sci.*, 2017, **10**, 2256–2266.
- 480 12 Y. Xiao, Y. Qian, A. Chen, T. Qin, F. Zhang, H. Tang, Z. Qiu and B.-L. Lin, *J. Mater.*  
481 *Chem. A*, 2020, **8**, 18310–18317.
- 482 13 B. Kim, H. Seong, J. T. Song, K. Kwak, H. Song, Y. C. Tan, G. Park, D. Lee and J. Oh,  
483 *ACS Energy Lett.*, 2020, **5**, 749–757.
- 484 14 T. A. Kistler, M. Y. Um, J. K. Cooper, I. D. Sharp and P. Agbo, *Adv. Energy Mater.*,  
485 2021, **11**, 2100070.
- 486 15 V. Andrei, B. Reuillard and E. Reisner, *Nat. Mater.*, 2020, **19**, 189–194.
- 487 16 T. Arai, S. Sato and T. Morikawa, *Energy Environ. Sci.*, 2015, **8**, 1998–2002.
- 488 17 M. Asadi, K. Kim, C. Liu, A. V. Addepalli, P. Abbasi, P. Yasaei, P. Phillips, A.  
489 Behranginia, J. M. Cerrato, R. Haasch, P. Zapol, B. Kumar, R. F. Klie, J. Abiade, L. A.  
490 Curtiss and A. Salehi-Khojin, *Science*, 2016, **353**, 467–470.
- 491 18 C. E. Creissen and M. Fontecave, *Adv. Energy Mater.*, 2020, **11**, 2002652.
- 492 19 L.-C. Weng, A. T. Bell and A. Z. Weber, *Energy Environ. Sci.*, 2019, **12**, 1950–1968.
- 493 20 C. M. Gabardo, C. P. O’Brien, J. P. Edwards, C. McCallum, Y. Xu, C.-T. Dinh, J. Li, E.  
494 H. Sargent and D. Sinton, *Joule*, 2019, **3**, 2777–2791.
- 495 21 J. F. Geisz, R. M. France, K. L. Schulte, M. A. Steiner, A. G. Norman, H. L. Guthrey, M.  
496 R. Young, T. Song and T. Moriarty, *Nat. Energy*, 2020, **32**, 326–335.
- 497 22 A. Royne, C. J. Dey and D. R. Mills, *Sol. Energy Mater. Sol. Cells*, 2005, **86**, 451–483.
- 498 23 A. Aldossary, S. Mahmoud and R. AL-Dadah, *Appl. Therm. Eng.*, 2016, **100**, 490–500.
- 499 24 G. Siefert and A. W. Bett, *Prog. Photovolt: Res. Appl.*, 2014, **22**, 515–524.
- 500 25 P. Singh and N. M. Ravindra, *Sol. Energy Mater. Sol. Cells*, 2012, **101**, 36–45.
- 501 26 A. Luque, *Solar cells and optics for photovoltaic concentration*, Adam Hilger, Bristol,  
502 1989.
- 503 27 T. A. Kistler, N. Danilovic and P. Agbo, *J. Electrochem. Soc.*, 2019, **166**, H656.
- 504 28 L.-C. Weng, A. T. Bell and A. Z. Weber, *Phys. Chem. Chem. Phys.*, 2018, **20**, 16973–  
505 16984.
- 506 29 J. S. DuChene, G. Tagliabue, A. J. Welch, X. Li, W.-H. Cheng and H. A. Atwater, *Nano*  
507 *Lett.*, 2020, **20**, 2348–2358.
- 508 30 D. M. Koshy, S. Chen, D. U. Lee, M. B. Stevens, A. M. Abdellah, S. M. Dull, G. Chen, D.  
509 Nordlund, A. Gallo, C. Hahn, D. C. Higgins, Z. Bao and T. F. Jaramillo, *Angew. Chem.*,  
510 2020, **132**, 4072–4079.
- 511 31 A. Goyal, G. Marcandalli, V. A. Mints and M. T. M. Koper, *J. Am. Chem. Soc.*, 2020, **142**,  
512 4154–4161.

- 513 32 M. Tahir, L. Pan, F. Idrees, X. Zhang, L. Wang, J.-J. Zou and Z. L. Wang, *Nano Energy*,  
514 2017, **37**, 136–157.
- 515 33 N.-T. Suen, S.-F. Hung, Q. Quan, N. Zhang, Y.-J. Xu and H. M. Chen, *Chem. Soc. Rev.*,  
516 2017, **46**, 337–365.
- 517 34 C. C. L. McCrory, S. Jung, I. M. Ferrer, S. M. Chatman, J. C. Peters and T. F. Jaramillo, *J.*  
518 *Am. Chem. Soc.*, 2015, **137**, 4347–4357.
- 519 35 P. Connor, J. Schuch, B. Kaiser and W. Jaegermann, *Z. Phys. Chem.*, 2020, **234**, 979–994.
- 520 36 S. Trasatti and O. A. Petrii, *Pure Appl. Chem.*, 1991, **63**, 711–734.
- 521 37 M. C. O. Monteiro, F. Dattila, B. Hagedoorn, R. García-Muelas, N. López and M. T. M.  
522 Koper, *Nat. Catal.*, 2021.
- 523 38 T. A. Kistler and P. Agbo, *APL Mater.*, 2020, **8**, 31107.
- 524 39 S. Nitopi, E. Bertheussen, S. B. Scott, X. Liu, A. K. Engstfeld, S. Horch, B. Seger, I. E. L.  
525 Stephens, K. Chan, C. Hahn, J. K. Nørskov, T. F. Jaramillo and I. Chorkendorff, *Chem.*  
526 *Rev.*, 2019, **119**, 7610–7672.
- 527 40 K. P. Kuhl, E. R. Cave, D. N. Abram and T. F. Jaramillo, *Energy Environ. Sci.*, 2012, **5**,  
528 7050.
- 529 41 W. Shockley and H. J. Queisser, *J. Appl. Phys.*, 1961, **32**, 510–519.
- 530 42 G. Lindquist, S. Oener, Q. Xu, A. R. Motz, A. Keane, C. Capuano, K. E. Ayers and S. W.  
531 Boettcher, *Meet. Abstr.*, 2020, **MA2020-02**, 2446.
- 532